

See discussions, stats, and author profiles for this publication at: <https://www.researchgate.net/publication/231646653>

# Magnesium Hydride Formation within Carbon Aerogel

ARTICLE in THE JOURNAL OF PHYSICAL CHEMISTRY C · JANUARY 2011

Impact Factor: 4.77 · DOI: 10.1021/jp1100768

CITATIONS

33

READS

25

8 AUTHORS, INCLUDING:



**Drew A Sheppard**

Curtin University

40 PUBLICATIONS 553 CITATIONS

SEE PROFILE



**Jim Webb**

Griffith University

43 PUBLICATIONS 382 CITATIONS

SEE PROFILE



**Evan Gray**

Griffith University

30 PUBLICATIONS 404 CITATIONS

SEE PROFILE



**C.E. Buckley**

Curtin University

105 PUBLICATIONS 1,628 CITATIONS

SEE PROFILE

# Magnesium Hydride Formation within Carbon Aerogel

Mark Paskevicius,<sup>†</sup> Hu-Yong Tian,<sup>†</sup> Drew A. Sheppard,<sup>†</sup> Colin J. Webb,<sup>‡</sup> Mark P. Pitt,<sup>‡</sup> Evan MacA. Gray,<sup>‡</sup> Nigel M. Kirby,<sup>§</sup> and Craig E. Buckley<sup>\*,†</sup>

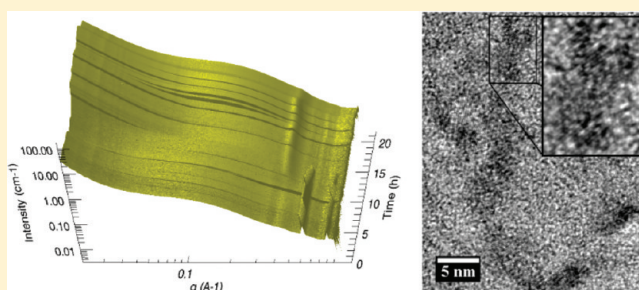
<sup>†</sup>Department of Imaging and Applied Physics, Curtin University of Technology, GPO Box U 1987, Perth, Western Australia 6845, Australia

<sup>‡</sup>Nanoscale Science and Technology Centre, Griffith University, Brisbane, Queensland 4111, Australia

<sup>§</sup>Australian Synchrotron, 800 Blackburn Road, Clayton, Victoria 3168, Australia

**S** Supporting Information

**ABSTRACT:** Magnesium hydride nanoparticles were synthesized within a carbon aerogel (CA) scaffold using a dibutylmagnesium precursor. The synthesis reaction was tracked using small-angle X-ray scattering (SAXS) to analyze the structural evolution during MgH<sub>2</sub> formation. The CA/MgH<sub>2</sub> composite was also investigated using X-ray diffraction (XRD) and transmission electron microscopy (TEM) to provide a better representation of the physical system. The CA has a large quantity of 2 nm pores as shown by nitrogen adsorption data. Both SAXS and TEM investigations confirm that MgH<sub>2</sub> does form within the 2 nm pores but XRD proves that there is also a significant quantity of larger MgH<sub>2</sub> particles within the system. Variations between hydrogen desorption isotherms from the CA/MgH<sub>2</sub> composite and bulk MgH<sub>2</sub> are detected that are indicative of changes in the decomposition properties of the small fraction of 2 nm MgH<sub>2</sub> nanoparticles within the CA/MgH<sub>2</sub> composite, changes which match theoretical predictions.



## INTRODUCTION

Magnesium hydride reversibly stores a theoretical maximum of 7.6 wt % of hydrogen and is currently undergoing intense research as a hydrogen storage material. The implementation of MgH<sub>2</sub> as a hydrogen storage material has been impeded by its high thermodynamic stability (i.e., MgH<sub>2</sub> must be heated to ~280 °C to obtain a hydrogen equilibrium pressure of 1 bar). Recent theoretical work<sup>1</sup> has suggested that reducing the particle size of MgH<sub>2</sub> below 10 nm will have an effect on the desorption temperature with the effect being pronounced below 3 nm.<sup>1–3</sup>

Based on this, a number of efforts have been made to produce nanosized, separated MgH<sub>2</sub> nanoparticles. Aguey-Zinsou et al.<sup>4</sup> and Kalidindi et al.<sup>5</sup> both produced surfactant-stabilized magnesium nanoparticles (<5 nm) suspended in a colloid. Aguey-Zinsou et al. obtained results that showed fast kinetics, even at 85 °C, as well as a possible change in the thermodynamics. However, it is likely that the change in thermodynamics can be attributed to the interaction of the stabilizing surfactant with the surface of the nanoparticles rather than to the size of the nanoparticles.<sup>6</sup> de Jongh et al.<sup>7</sup> successfully synthesized Mg nanoparticles within a variety of porous frameworks with Mg particle sizes ranging from a few nanometers in size down to 1 nm using a melt infiltration technique (up to Mg loadings of ~15 wt %). Despite synthesizing Mg particles in the size range predicted to have thermodynamic changes, no hydrogen measurements were performed. Gross et al.<sup>8</sup> and Bogerd et al.<sup>9</sup> also used the magnesium melt

infiltration technique by first doping carbon aerogels with nickel or copper to increase the loading level of magnesium by improving its liquid wetting properties. In these cases the carbon aerogel pore sizes (13 nm and <20 nm) were larger than the sizes predicted for thermodynamic changes to occur in the Mg–H system. Gross et al.<sup>8</sup> performed one equilibrium desorption measurement at 250 °C and found no discernible difference to bulk MgH<sub>2</sub> while Bogerd et al.<sup>9</sup> showed changes in the temperature-programmed desorption (TPD) spectra that can be assigned to either improved kinetics of the system or the formation of nonstoichiometric Mg–Ni compounds. MgH<sub>2</sub> nanoparticles have also been synthesized and confined using carbon aerogels, imbued using a dibutylmagnesium precursor. Magnesium hydride is then formed by the reduction of the dibutylmagnesium with hydrogen via the reaction<sup>10,11</sup>



Zhang et al.<sup>11</sup> used carbon aerogels with 13 nm pores, and Nielsen et al.<sup>10</sup> used carbon aerogels with 7 and 22 nm pores. No thermodynamic measurements were performed, but the absorption and desorption kinetics of these samples were superior to

**Received:** October 21, 2010

**Revised:** December 15, 2010

**Published:** January 12, 2011

bulk  $\text{MgH}_2$ . However, these kinetics were still substantially slower than for  $\text{MgH}_2$  ball-milled with a  $\text{Nb}_2\text{O}_5$  catalyst.<sup>12</sup>

Magnesium hydride has previously been confined within porous carbons<sup>8,10,11</sup> to study kinetic or thermodynamic benefits to nanoscopic  $\text{MgH}_2$ . This work clearly demonstrates the kinetic improvement of hydrogen desorption rates at relatively low temperatures ( $\sim 250^\circ\text{C}$ ) for nanoscopic  $\text{MgH}_2$ . However no definitive proof of changes to the thermodynamics of the  $\text{Mg-H}$  system has been shown in these carbon-supported systems to date. The lack of any thermodynamic destabilization is due to the resulting  $\text{MgH}_2$  particle size, which in these cases is typically larger than the critical threshold for any discernible thermodynamic changes to be observed. Small thermodynamic changes in the  $\text{Mg-H}$  system have been observed by the authors<sup>13</sup> in mechanochemically synthesized  $\text{MgH}_2$  particles ( $<7\text{ nm}$ ) embedded within a salt matrix.<sup>14</sup>

One recurring theme in the synthesis of the  $\text{Mg-carbon}$  nanocomposites is the difficulty in characterizing the samples. For samples with low loadings of  $\text{Mg/MgH}_2$ , XRD shows an absence of diffraction peaks<sup>7,8</sup> (and hence a crystallite size cannot be determined). Samples with higher loadings of  $\text{Mg/MgH}_2$  contain both nanosized  $\text{Mg/MgH}_2$  and larger bulklike  $\text{MgH}_2$ . The resulting XRD patterns are then completely dominated by bulk  $\text{Mg/MgH}_2$ . TEM also produces ambiguous results on the particle size and distribution owing to the low contrast between the  $\text{MgH}_2$  nanoparticles and the carbon support.<sup>8,11</sup>

In order to investigate thermodynamic changes in the  $\text{Mg-H}$  system, a carbon aerogel with sub-10 nm pores was synthesized and used as a scaffold. The carbon aerogel serves two purposes: first, it provides an array of discrete sites where the  $\text{MgH}_2$  particles can form, and second, these sites are separated by a carbon framework that restricts the growth of the  $\text{MgH}_2$  particles. Thus, after the  $\text{MgH}_2$  has been formed, a proportion will be trapped within the carbon aerogel pore structure. The thermodynamics of the  $\text{Mg-H}$  system can then be investigated by careful hydrogen sorption measurements taking into consideration that there will be  $\text{MgH}_2$  in the small pores but also bulklike  $\text{MgH}_2$  in any pores  $>10\text{ nm}$ . To date there has been no firm evidence that a large fraction of the  $\text{MgH}_2$  is actually confined within the carbon aerogel pore structure, likely due to the difficulties in obtaining clear images of this system with transmission electron microscopy (TEM). A combination of in situ small-angle X-ray scattering (SAXS) and TEM is undertaken in the present work to provide a better understanding of this composite system.

## ■ EXPERIMENTAL SECTION

**Sample Preparation.** Carbon aerogels (CA) were prepared from resorcinol (99%), furfural (99%), and hexamethylenetetramine (99%), which were all obtained from Sigma Aldrich Pty. Ltd., Australia. The CA synthesis procedure is detailed elsewhere.<sup>15</sup> Briefly, CAs were synthesized by an acetic acid catalyzed pathway from resorcinol and furfural, followed by ambient pressure drying for 4 h. The dried gels were then carbonized at  $900^\circ\text{C}$  for 3 h under a flowing  $\text{N}_2$  atmosphere, followed by activation at  $1000^\circ\text{C}$  for 1 h under a flowing  $\text{CO}_2$  atmosphere. It should be noted that CAs synthesized by ambient pressure drying are often referred to as xerogels in the literature, but given that the carbon structure in these samples is more akin to aerogels, the samples have been referred to as CA. The pure CA was physically mixed with an as-received 1 M dibutylmagnesium

solution suspended in heptane (Sigma Aldrich) within an Ar-filled glovebox to prevent oxygen and moisture contamination. The physical mixture was then centrifuged under 2000g for 4 h to draw the  $\text{MgBu}_2$  into the CA structure. The sample was then dried for 3–7 days at ambient temperature under flowing argon to remove all traces of heptane. A purchased  $\text{MgH}_2$  (Sigma-Aldrich,  $\geq 96.5\%$ ) powder sample was prepared as a “bulk” reference material for hydrogen sorption experiments. The purchased  $\text{MgH}_2$  was ball milled for 18 h using a ball to powder ratio of 90:1 in order to improve the reaction kinetics before use.

**Instrumentation.** In situ SAXS patterns were collected on the SAXS/WAXS beamline at the Australian Synchrotron with a high-intensity undulator source. The X-ray energy was chosen as 20 keV in order to observe a  $q$ -range of  $0.02\text{--}1.0\text{ \AA}^{-1}$  using a Pilatus 1 M detector with a sample to detector distance of 1612 mm. Patterns were collected with 5–10 s collection times and were processed and background corrected using the SAXS15ID software package.<sup>16</sup> All patterns were then scaled to absolute intensity using a known calibration procedure with glassy carbon.<sup>17</sup> During SAXS data collection the sample was placed within a high-pressure X-ray diffraction cell designed specifically for solid–gas reactions.<sup>18</sup> The cell was connected to a Sieverts’ manometric apparatus that enabled the sample to be heated from room temperature to  $175^\circ\text{C}$  under hydrogen pressures from vacuum to 20 bar while SAXS patterns were collected.

Additional SAXS data sets were acquired for a sample of pure carbon aerogel to conclusively separate heating effects on the aerogel from changes in dibutylmagnesium and magnesium hydride. These SAXS patterns were recorded with a Bruker Nanostar SAXS instrument at Curtin University utilizing a custom-made heating stage. Data were recorded at  $175^\circ\text{C}$  at a detector distance of 23.2 cm using a wavelength,  $\lambda$ , of  $1.5418\text{ \AA}$  ( $\text{Cu K}\alpha$ ) with a 2D multiwire detector. The raw pattern was radially averaged and the background subtracted, with the resulting data sets spanning the  $q$ -range of  $0.153\text{--}0.837\text{ \AA}^{-1}$ .

The nitrogen adsorption isotherm was measured gravimetrically with a QuadraSorb Station 4 at 77 K. The sample was evacuated at  $200^\circ\text{C}$  for 4 h prior to the adsorption measurements.

Transmission electron microscopy (TEM) was conducted on a JEOL 3000F FEGTEM instrument operating at 300 kV. Samples were loaded onto 200-mesh copper grids with holey carbon support films dropwise via suspension in toluene. Samples were exposed to air before being loaded into the TEM column; however, the air exposure time was kept as short as possible (up to a few minutes).

X-ray diffraction (XRD) was performed using a Bruker D8 Advance diffractometer ( $\text{Cu K}\alpha$  radiation) with a  $2\theta$  range of  $10^\circ\text{--}100^\circ$  using  $0.02^\circ$  steps with 0.8 s of count time per step with operating conditions of 40 kV and 40 mA. The XRD instrument was equipped with a LynxEye 3° linear position sensitive detector (PSD) with 192 pixels. The instrumental line broadening is taken into account using a fundamental parameters approach in Topas (Bruker AXS) that was verified using a NIST 660a  $\text{LaB}_6$  reference standard. The sample was loaded into an XRD sample holder in an argon glovebox and sealed with a poly(methyl methacrylate) (PMMA) airtight bubble to prevent oxygen/moisture contamination during data collection. The crystallite sizes were determined from an LVol-IB method (volume averaged column height calculated from the integral breadth)<sup>19</sup> that provides a good measure of the volume-weighted average crystallite size.

Temperature-programmed desorption (TPD) or differential scanning calorimetry (DSC) is commonly used to characterize  $\text{MgH}_2$  systems. However, claims of lowering the desorption temperature<sup>20–22</sup> are often incorrect due to the failure to correctly separate the kinetic and thermodynamic components of the TPD/DSC signal.<sup>23</sup> Claims of reductions in the desorption temperature are in fact a reduction in the activation energy of desorption<sup>24</sup> and hence have no influence on the thermodynamics of the system. If the kinetic limitations of the  $\text{MgH}_2$  system could be completely removed, TPD performed under vacuum or flowing argon would result in hydrogen evolution below 100 °C. Rongeat et al.<sup>23</sup> outline a method for using both the absorption and desorption DSC curve for a sample. Using this method, Rongeat et al. determined that the enthalpy of  $\text{MgH}_2$  was between 80.8 kJ/mol  $\text{H}_2$  and 68.1 kJ/mol  $\text{H}_2$ . Using a slower heating rate for kinetically limited systems such as  $\text{MgH}_2$  may reduce this level of uncertainty, but it is unclear if it is sufficient to establish the small changes in thermodynamics that are expected for nanosized  $\text{MgH}_2$ .

Alternatively, the thermodynamics can be determined from a series of pressure–composition–temperature (PCT) curves performed at different temperatures. PCT curves can determine thermodynamic quantities to a higher accuracy but only if the following protocols are adhered to: (1) that adequate time transpires for each equilibrium measurement to ensure the system is at equilibrium and (2) that PCT curves are performed at a minimum of four different temperatures. Ensuring that the system is at equilibrium at each data point in a PCT curve can avoid hysteresis or sloping plateaus that are purely an artifact of slow kinetics, a problem that regularly occurs within the literature.<sup>25,26</sup>

Ex situ hydrogen sorption experiments were performed in a Sieverts' manometric apparatus. Further details regarding this particular apparatus can be found elsewhere.<sup>13</sup> All hydrogen measurements used long equilibrium times to ensure true equilibrium was obtained (3 h for bulk  $\text{MgH}_2$  and 24 h for as-prepared CA/ $\text{MgH}_2$ ). Kinetic curves for these samples (see Supporting Information) confirm that the samples have reached equilibrium for each measurement (with the exception of 3–5 data points as discussed in the text). Temperature-programmed desorption (TPD) was performed on a PCT-Pro E&E (Hy-Energy) coupled to a quadrupole mass spectrometer Residual Gas Analyzer (Stanford Research Systems RGA 300). The sample was first outgassed at  $3 \times 10^{-7}$  bar and 25 °C for 6 h. While still under vacuum, the sample was heated up to 380 °C at a heating rate of 1 °C/min at which point the heating was halted and the sample allowed to cool to room temperature.

## RESULTS AND DISCUSSION

**Carbon Aerogel.** The pure CA was analyzed using nitrogen adsorption as shown in Figure 1. A theoretical model based on DFT<sup>27</sup> was used to determine the pore volumes where it was found that the CA contains 0.69  $\text{cm}^3/\text{g}$  of micropores (0–2 nm) and 0.61  $\text{cm}^3/\text{g}$  of mesopores (2–20 nm). The starting aerogel was synthesized by a subcritical procedure using acetic acid as a catalyst in order to form high concentrations of micropores. The high concentration of micropores provides more sites for sub-2 nm  $\text{MgH}_2$  to form.

**In Situ SAXS.** The in situ SAXS experiment was designed to examine the structural changes in the CA system during  $\text{MgH}_2$  formation from the dibutylmagnesium ( $\text{MgBu}_2$ ) precursor.

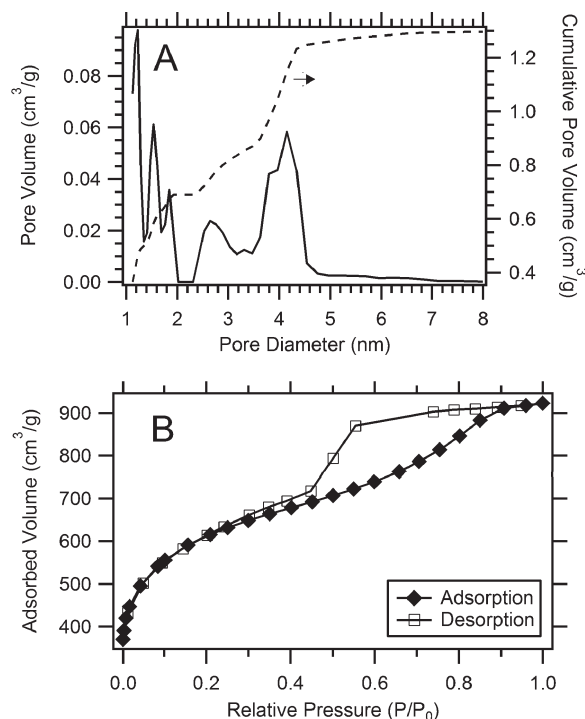


**Figure 1.** Nitrogen adsorption data for pure CA. (A) The calculated pore volume (DFT model) is displayed along with (B) the raw adsorption/desorption data.

Gas pressure data was collected as the reduction reaction progressed, but it does not provide adequate information to detect reaction completeness. This is because as hydrogen is depleted by its reaction with  $\text{MgBu}_2$  the butane gas byproduct results in a static system pressure. The in situ decomposition of  $\text{MgBu}_2$  and formation of  $\text{MgH}_2$  within the CA structure is illustrated by the SAXS plots in Figure 2. The CA/ $\text{MgBu}_2$  sample was initially placed under 4 bar of hydrogen pressure at 50 °C. The SAXS pattern shows a power law at low  $q$ , followed by a Guinier regime and another power law at high  $q$ . These scattering features result from the carbon aerogel structure itself and are described quantitatively below. There is a slight hump in the high- $q$  power law at  $q = 0.47 \text{ \AA}^{-1}$  that may be due to  $\text{MgBu}_2$  confined within the pores of the CA but it is difficult to confirm this hypothesis. The similarity in electron density between CA and  $\text{MgBu}_2$  may also account for the weak nature of this hump. Diffraction peaks are present at  $q = 0.634$  and  $0.892 \text{ \AA}^{-1}$  from  $\text{MgBu}_2$  where the high- $q$  peak is at an identical position to previous work.<sup>10</sup>

The sample temperature was stepped up to 100 °C at point A in Figure 2 with no major structural changes detectable. However a slight reduction in the intensity of the  $\text{MgBu}_2$  diffraction peaks is observed, indicating that the reaction between the  $\text{H}_2$  gas and the  $\text{MgBu}_2$  will progress but is kinetically limited at low pressures (<4 bar) and temperatures (<100 °C). Consequently, to increase the kinetics of the reaction, the sample was heated to 125 °C at point B. The increase in temperature leads to a further reduction in the  $\text{MgBu}_2$  peak intensity, indicating a decomposition of this phase due to butane formation as given by reaction 1. A broad peak at  $q = 0.44 \text{ \AA}^{-1}$  quickly grows in size corresponding to the decrease in the intensity of the  $\text{MgBu}_2$  diffraction peaks. This broad peak is associated with the formation of  $\text{MgH}_2$  nanoparticles within the ~2 nm CA pores and is quantitatively modeled below. A SAXS



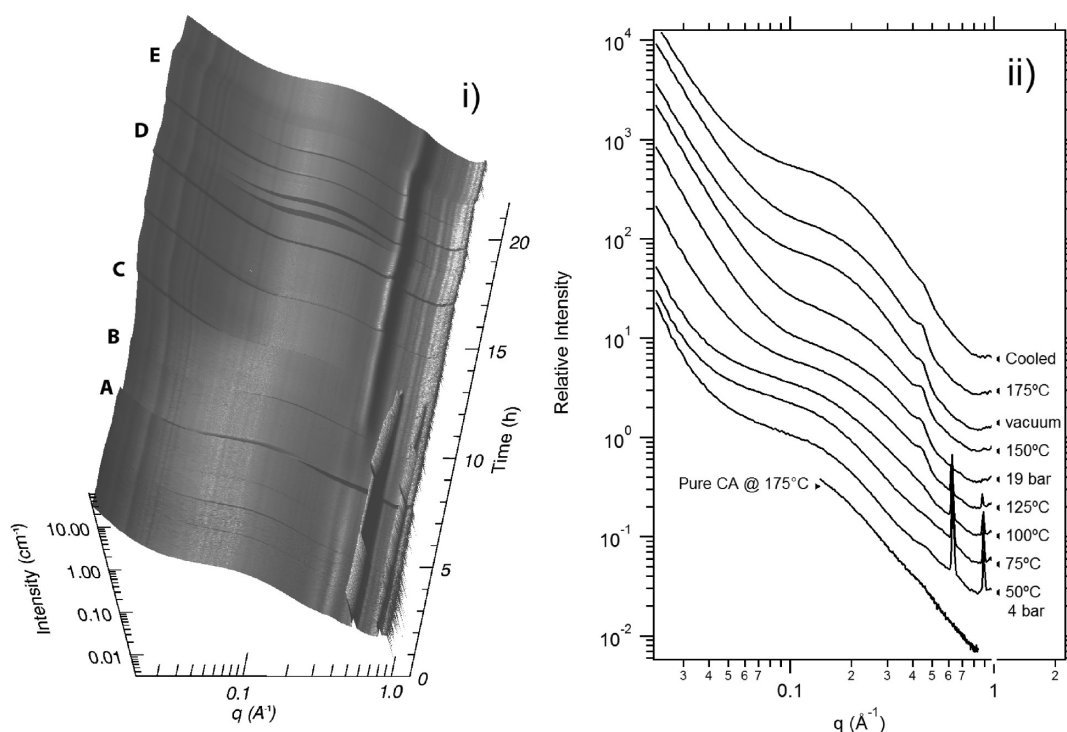


**Figure 2.** In situ SAXS patterns collected during  $\text{MgH}_2$  formation within carbon aerogel from a butyl magnesium precursor. (i) A surface plot and (ii) a cross section of SAXS patterns are displayed. The alphabetical labels are notable points as described in the text, and patterns have been offset for clarity in (ii).

pattern was collected at 175 °C for pure CA (as shown in Figure 2, ii) to verify that the broad peak at  $q = 0.44 \text{ \AA}^{-1}$  is not simply due to temperature-induced structural changes in pure CA. No broad hump is detected in the heated CA and thus it can be attributed solely to the  $\text{MgH}_2$  nanoparticles.

The sample is subjected to 19 bar of  $\text{H}_2$  pressure at point C and all traces of  $\text{MgBu}_2$  are immediately reduced. The sample is stepped down to vacuum at point D, resulting in an increased intensity of the Guinier region at  $q = 0.15 \text{ \AA}^{-1}$ . The dependence of the Guinier region intensity upon pressure of the system in fact demonstrates that this Guinier region is generated from the CA pore structure. The Guinier region exists due to the scattering length density difference between the carbon network in the CA and the pores, known as the scattering contrast. If the pores are empty, then the scattering contrast is equal to the scattering length density of the carbon, but if the pores are filled with  $\text{H}_2$  and  $\text{C}_4\text{H}_{10}$ , then the scattering contrast is reduced in intensity due to the smaller scattering length density difference between the carbon and the filled pores. Hence an evacuation of the gas in the system leads to a change in the scattering contrast of the pores and an increase in the intensity of the associated Guinier region. Butane is known to condense within porous carbon structures even at elevated temperatures<sup>28</sup> and the scattering length density difference between carbon ( $\rho = 16.1 \times 10^{10} \text{ cm}^{-2}$ ) and liquid butane at 150 °C ( $\rho = 3.0 \times 10^{10} \text{ cm}^{-2}$ ) can account for the intensity increase of the Guinier region upon evacuation. The sample is cooled down to room temperature at point E resulting in a shift in the Guinier shoulder due to a thermal relaxation of the CA structure. This relaxation causes the  $\text{MgH}_2$  peak to become less obvious but it remains present until the sample reaches near-ambient temperature.

The SAXS scattering patterns from the CA/ $\text{MgBu}_2$  system can be described using the following function:

$$I(q) = B_A \exp\left(\frac{-q^2 R_{\text{GB}}^2}{3}\right) q^{-P_A} + G_B \exp\left(\frac{-q^2 R_{\text{GB}}^2}{3}\right) + B_B \left\{ \frac{[\text{erf}(q R_{\text{GB}}/\sqrt{6})]^3}{q} \right\}^{P_B} + I_{\text{PHS}} \quad (2)$$

The scattering intensity is a function of the scattering vector,  $q = 4\pi \sin(2\theta)/\lambda$ , where  $\lambda$  is the wavelength (0.8271 Å) and  $\theta$  is the scattering angle. The scattering function is primarily based upon the unified model that was constructed by Beaucage<sup>29</sup> in order to accurately model the CA structure. The first term in eq 2 is a low- $q$  power law regime with a high- $q$  cutoff, the second term is a Guinier regime, and the third term is a high- $q$  power law regime with a low- $q$  cutoff implemented by the error function,  $\text{erf}(x) = [2/(\pi)^{1/2}] \int_0^x e^{-t^2} dt$ . The unified model implements cutoffs to realistically separate scattering regimes from one another due to a structural feature's finite length scale in a physical system. The low- $q$  power law is described by a scattering prefactor,  $B_A$ , and a power law exponent,  $P_A$ , that describe surface fractal scattering in the case of CA. The high- $q$  power law is similarly described by a scattering prefactor,  $B_B$ , and a power law exponent,  $P_B$ , but instead describes mass fractal scattering from the pore network within the CA. The Guinier regime models the scattering from the pores in the CA where  $G_B$  is an exponential prefactor based on the scattering power of the system and  $R_{\text{GB}}$  is the radius of gyration of the pores (the exact relationship between  $R_{\text{GB}}$  and a physically meaningful structure depends on the assumed shape of the structure). The scattering function also

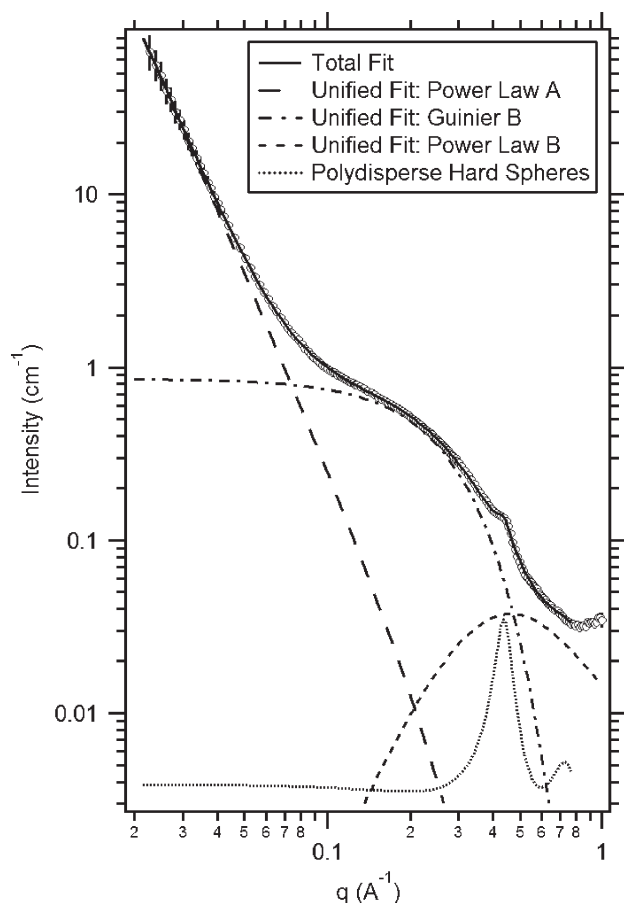


**Figure 3.** Typical model fit to SAXS data set from a 125 °C measurement. The individual model components are also displayed to better describe the different parts of the SAXS scattering pattern.

includes the polydisperse sphere model ( $I_{\text{PHS}}$ ) describing scattering from  $\text{MgH}_2$  particles within the CA pores that is based upon work by Griffith et al.<sup>30</sup> Both the unified model and polydisperse sphere model were combined into a single custom scattering function using the NIST Center for Neutron Research (NCNR) SANS macros<sup>31</sup> for the Igor Pro software package (Wavemetrics, USA). A typical fit to the data by eq 2 is provided in Figure 3 demonstrating an extremely good fit to the SAXS data set. Quantitative data resulting from fits to each data set in Figure 2(ii) are provided in Table 1.

The quantitative data in Table 1 provides insight into the formation mechanism of the  $\text{MgH}_2$  and verifies its presence in sub-2 nm CA pores. First, the scattering from the CA was modeled using the unified equation and displays slight structural differences under different temperature and pressure conditions. The power law slope at low- $q$  is typical of the surface fractal scattering regime (given by  $P_A$  as 3.6–3.7), demonstrating that the CA maintains a constant rough surface during  $\text{MgH}_2$  deposition. The surface scattering from large structural features in the CA is strongly correlated with temperature indicated by an increase in  $B_A$  whenever the sample temperature is increased. However,  $B_A$  also displays a correlation with pressure. The power law scattering exponent,  $B_A$ , is a function of the volume of the large CA particle structure that results in surface scattering.

The micropores within the CA are modeled by the Guinier regime within the unified equation. The exponential prefactor,

$G_B$ , can be related to the scattering contrast between the carbon and the material within the pore. In a complex fashion,  $G_B$  provides an indication of CA pore occupation. The scattering contrast is made complicated by the fact that the pores may contain hydrogen,  $\text{MgBu}_2$ , butane,  $\text{MgH}_2$ , or vacuum. The final structural feature from the CA is the high- $q$  power law that describes the aggregate micropore structure by a mass fractal scattering regime. The micropore aggregate within the CA remains relatively stable throughout the in situ experiment and any quantitative analysis is made difficult due to the short  $q$ -range in which the power law exists due to a high scattering background above  $q = 0.8 \text{ \AA}^{-1}$ .

The polydisperse sphere model ( $I_{\text{PHS}}$ ) was used to analyze scattering from the synthesized  $\text{MgH}_2$  nanoparticles within the CA micropores. Particle diameter ( $D$ ), polydispersity, and the volume fraction of  $\text{MgH}_2$  in the pores are all determined from the fit to the scattering data (see Table 1). The  $\text{MgH}_2$  particle size increases until the sample is raised to 150 °C, indicating growth of the particles as they are formed by the reduction of  $\text{MgBu}_2$  given by eq 1. The  $\text{MgH}_2$  particle growth is matched by an increase in the volume fraction of  $\text{MgH}_2$  within the pores until the sample reaches 150 °C. After the sample is heated above this temperature and is exposed to vacuum, a decrease in both  $\text{MgH}_2$  particle size and volume fraction is detected. This phenomenon cannot be known definitively from SAXS data alone but migration of  $\text{MgH}_2$  at high temperatures and low pressures from the CA micropores to the mesopores cannot be ruled out. Despite the reduction in the volume fraction of  $\text{MgH}_2$  in the micropores, a significant quantity is detected from the SAXS data that is sub-2 nm in size from the fit to the hump in the SAXS patterns at  $q = 0.4\text{--}0.5 \text{ \AA}^{-1}$  using the polydisperse sphere model.

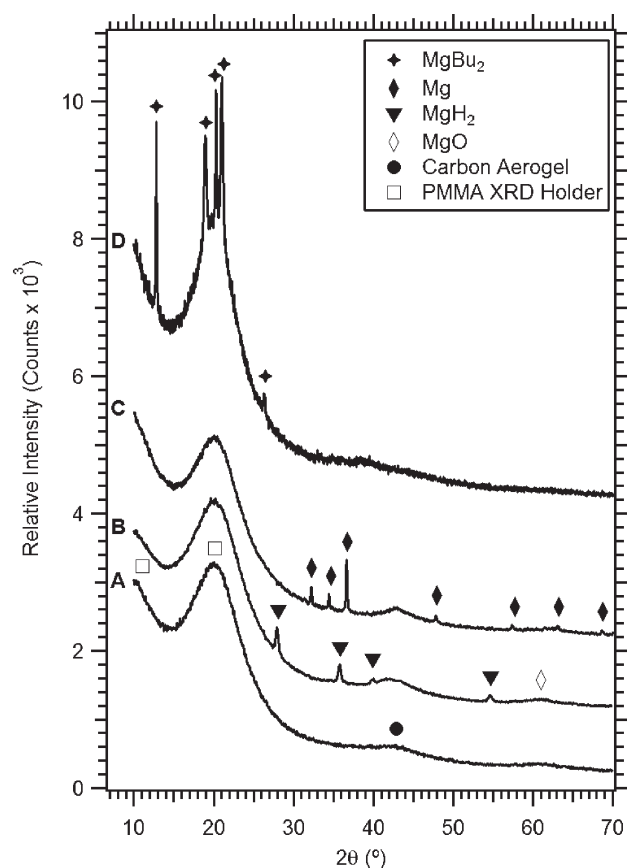
**Diffraction and TEM.** XRD data provided in Figure 4 illustrates the evolution of the CA/ $\text{MgBu}_2$  system. Initially, the as-prepared CA/ $\text{MgBu}_2$  sample only displays a CA signature in the XRD pattern (Figure 4A) and the  $\text{MgBu}_2$  cannot be detected with the lab-based diffractometer (D8 Advance) due to the low concentration of the  $\text{MgBu}_2$  phase. It is also possible that the  $\text{MgBu}_2$  peaks are hidden by the broad PMMA peaks from the XRD holder. Once the  $\text{MgBu}_2$  has been reduced by hydrogen, the XRD pattern (Figure 4B) reveals that  $\text{MgH}_2$  has been synthesized with an average crystallite size of 16 nm. To be clear, this is not the particle size, which can be much larger, constructed from multiple crystallites. It is apparent from the large crystallite size that not all the  $\text{MgH}_2$  is confined within the micropores. It is likely that a large concentration of  $\text{MgH}_2$  exists within both the meso- and macropores with pore sizes >2 nm. This result is consistent with the synthesis technique as the original  $\text{MgBu}_2$  would have deposited throughout the entire CA network. Upon desorption at 300 °C the XRD pattern (Figure 4C) reveals a complete transformation from  $\text{MgH}_2$  to Mg with an average crystallite size of 55 nm. The significant increase in crystallite size may be due to annealing where multiple crystallites sinter to form single crystals within their associated pores; however, it is likely that significant agglomeration occurs between Mg particles that reside within large macropores >50 nm. In addition, XRD data is volume weighted, meaning the peaks generated for the  $\text{MgH}_2$  are significantly biased toward the diffraction from larger crystallites due to their large volumes.

The XRD data in conjunction with the SAXS data depict a CA network containing  $\text{MgH}_2$  particles trapped within micropores (sub-2 nm) along with much larger bulk  $\text{MgH}_2$  that exists within the large CA pore structure. This explanation of the CA/ $\text{MgH}_2$

Table 1. SAXS Fitting Results to Data Provided in Figure 2(ii)<sup>a</sup>

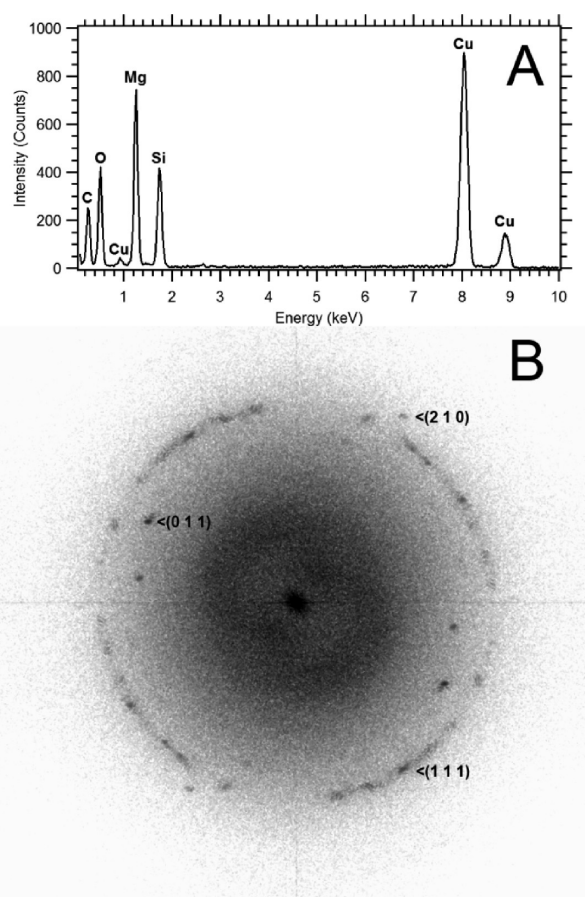
sample conditions	carbon aerogel						MgH <sub>2</sub>		
	$B_A$ (cm <sup>-1</sup> Å <sup>-P<sub>A</sub></sup> )	$P_A$	$G_B$ (cm <sup>-1</sup> )	$R_{gB}$ (Å)	$B_B$ (cm <sup>-1</sup> Å <sup>-P<sub>B</sub></sup> )	$P_B$	$D$ (Å)	polydisp.	vol fraction
50 °C/4 bar	$4.4 \times 10^{-6}$	4.0	1.5	10	0.017	1.9	—	—	—
75 °C	$9.9 \times 10^{-6}$	3.7	1.7	10	0.021	1.9	—	—	—
100 °C	$1.0 \times 10^{-5}$	3.7	1.3	10	0.014	1.9	12	0.3	0.2
125 °C	$4.0 \times 10^{-5}$	3.6	0.98	7.7	0.007	1.9	14	0.3	0.5
19 bar	$6.0 \times 10^{-5}$	3.7	0.86	6.5	0.014	1.9	18	0.1	0.8
150 °C	$9.9 \times 10^{-5}$	3.6	1.1	6.9	0.017	1.9	18	0.1	0.7
vacuum	$7.1 \times 10^{-5}$	3.7	2.3	7.9	0.013	1.9	16	0.2	0.6
175 °C	$1.0 \times 10^{-4}$	3.7	2.5	7.8	0.020	1.9	16	0.1	0.6
cooled	$6.5 \times 10^{-5}$	3.6	2.7	8.2	0.013	1.9	14	0.2	0.4

<sup>a</sup> The fitted parameters arise from eq 2 and refer to the low- $q$  scattering prefactor ( $B_A$ ) and power law exponent ( $P_A$ ), the exponential prefactor ( $G_B$ ) and radius of gyration ( $R_{gB}$ ), the high- $q$  scattering prefactor ( $B_B$ ) and power law exponent ( $P_B$ ), and the particle diameter of MgH<sub>2</sub> ( $D$ ) including its polydispersity and volume fraction within each pore. The uncertainty on each value is equal to  $\pm 1$  in the final significant figure.



**Figure 4.** XRD patterns for a carbon aerogel sample (A) doped with MgBu<sub>2</sub> which is then (B) reduced with hydrogen at 170 °C and then (C) desorbed at 300 °C. Also displayed is (D) pure MgBu<sub>2</sub>.

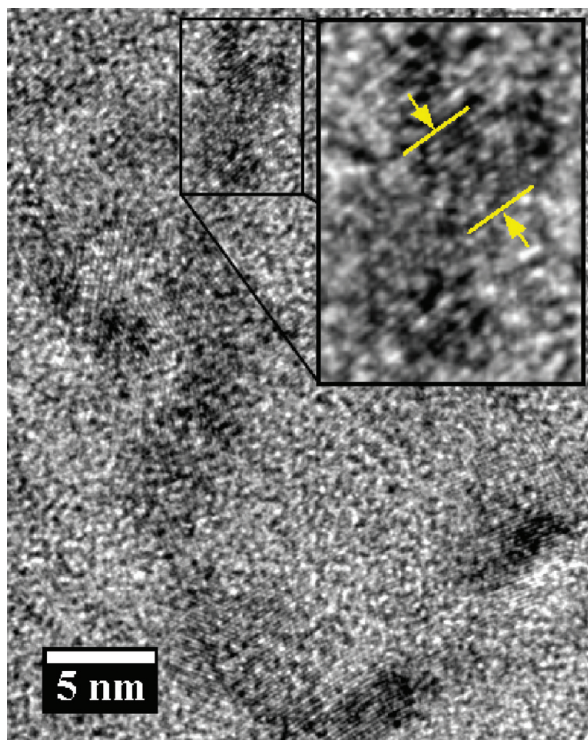
system is also reinforced by TEM investigations. First, TEM imaging of the CA/MgH<sub>2</sub> system was difficult. The MgH<sub>2</sub> particles do not provide enough electron contrast and can be difficult to discern from the CA structure as found in other studies.<sup>11</sup> The detection of MgH<sub>2</sub> was undertaken using two methods. Energy-dispersive spectroscopy was used to identify the presence of Mg (as shown in Figure 5A); however, the primary method of MgH<sub>2</sub> detection was imaging the lattice fringing from the particles embedded within the CA matrix.



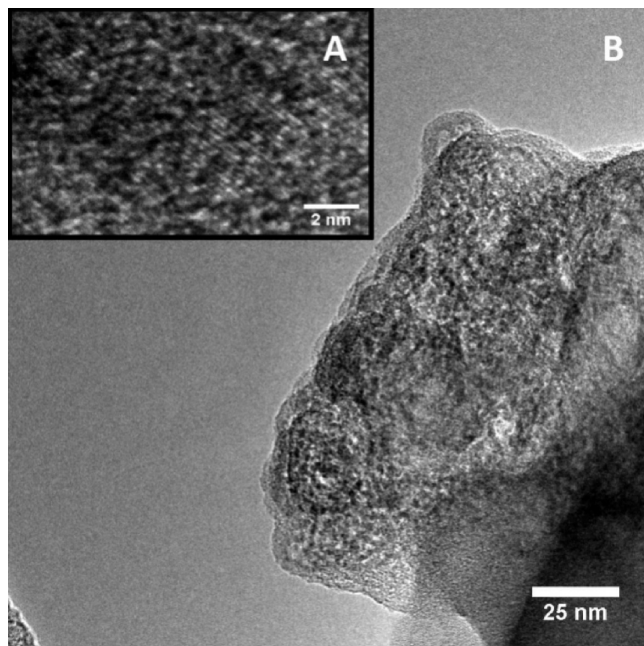
**Figure 5.** (A) Energy-dispersive spectroscopy (EDS) and (B) FFT pattern from TEM investigations of the CA/MgH<sub>2</sub> system.  $hkl$  indexing is provided for MgH<sub>2</sub>. Si and Cu are present in the EDS from the TEM grid, and O is present due to air exposure.

Figure 5B displays a FFT image from a typical TEM image of the CA/MgH<sub>2</sub> system where lattice fringing was detected. The FFT provides a  $hkl$  spot pattern akin to electron diffraction for the MgH<sub>2</sub> within the CA. A set of radial profiles used for indexing is provided in the Supporting Information. The spatial ( $d$ ) resolution and accuracy is not as high as other techniques such as XRD but it is sufficient for  $hkl$  indexing a particular phase.





**Figure 6.** TEM micrograph of dark regions displaying  $\text{MgH}_2$  lattice fringing within the CA matrix. The inset provides a magnified view ( $2.2\times$ ) of one of the darker regions with lattice fringing.



**Figure 7.** TEM micrographs of (A) larger  $\text{MgH}_2$  crystals and (B) small  $\text{MgH}_2$  particles (black dots) within the CA matrix.

Direct TEM images are provided in Figures 6 and 7. The sample is dominated by a speckled pattern from the CA pore network. Within the CA structure are darker (black) regions that do correlate well with the presence of  $\text{MgH}_2$ . Figure 6 shows a high-resolution image of 5 nm dark regions within the CA

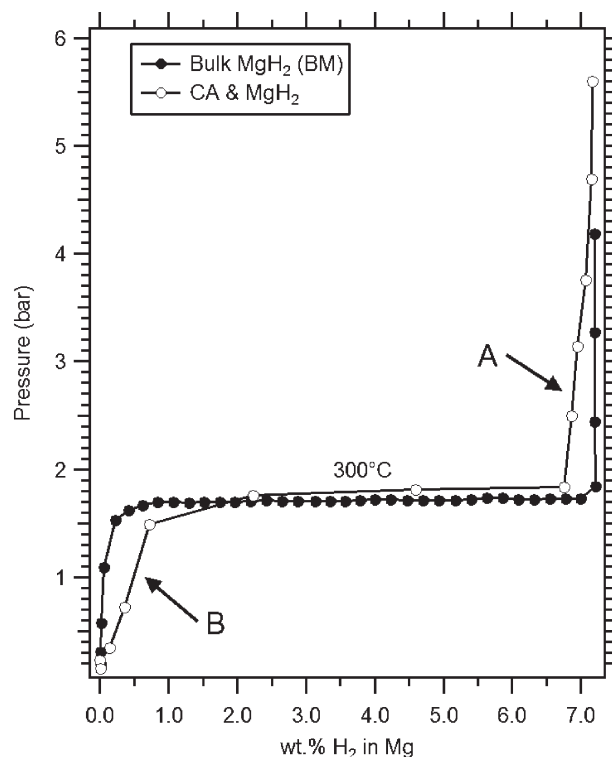


**Figure 8.** Pressure–composition isotherms (PCI) collected at 300 °C comparing desorption data for pure “bulk”  $\text{MgH}_2$  and the CA/ $\text{MgH}_2$  composite. The CA/ $\text{MgH}_2$  wt % was calculated assuming full desorption. A and B refer to deviations in the PCI that have been attributed to thermodynamic changes in  $\text{MgH}_2$  with particle size as described in the text.

network. Each of these darker regions displays significant lattice fringing from  $\text{MgH}_2$ . A similar phenomenon is depicted in Figure 7A for a larger dark region, where again lattice fringing from  $\text{MgH}_2$  was detected from an interplanar spacing of 2.2 Å being measured, consistent with the  $\text{MgH}_2$   $hkl = 111$  plane at 2.19 Å. A larger section of the CA/ $\text{MgH}_2$  composite is displayed in Figure 7B where a multitude of 2 nm dark  $\text{MgH}_2$  regions are dispersed throughout the pore network. Therefore, TEM investigations reinforce the SAXS results by detecting the presence from small  $\text{MgH}_2$  particles that are trapped within the CA pore network.

**Hydrogen Sorption.** Hydrogen pressure–composition isotherms (PCI) are collected at 300 °C in order to detect changes in the CA/ $\text{MgH}_2$  system. It is extremely difficult to accurately detect these changes by other means as most other techniques (i.e., TPD or DSC) include a misleading kinetic component. It should be noted that the sorption kinetics of the CA/ $\text{MgH}_2$  sample were significantly slower than the ball-milled bulk sample of  $\text{MgH}_2$ . Each PCI data point for the CA/ $\text{MgH}_2$  sample was collected over 24 h whereas only 3 h were required for the bulk sample to reach equilibrium. It is not entirely clear why the CA/ $\text{MgH}_2$  sample has such poor kinetics as reaction kinetics are expected to quicken with the increase in  $\text{MgH}_2$  surface area. Other studies have reported fast sorption kinetics for CA/ $\text{MgH}_2$  composites,<sup>10,11</sup> however, in these cases the CA/ $\text{MgH}_2$  sorption kinetics are still significantly slower than  $\text{MgH}_2$  samples that have been ball milled, where desorption from the CA/ $\text{MgH}_2$  composites is still not complete after 7 h.<sup>10,11</sup> The reason for slow reaction kinetics in CA/ $\text{MgH}_2$  samples may be due to a high



quantity of carbon in the Mg–H system. Such a large quantity of carbon encasing the  $\text{MgH}_2$  could result in slow hydrogen migration through the complex carbon network. Zhang et al.<sup>11</sup> synthesized a “bulk”  $\text{MgH}_2$  sample that was ball milled with 84 wt % graphite flakes and showed that the desorption kinetics of this sample were very slow where the sample was still desorbing after 48 h at 252 °C. However, small quantities of carbon materials have been previously shown to increase the reaction kinetics of the  $\text{MgH}_2$  system.<sup>32</sup> Alternatively, sorption kinetics for bulk  $\text{MgH}_2$  are notoriously slow and XRD indicates that a large quantity of bulk  $\text{MgH}_2$  is present within the CA/ $\text{MgH}_2$  sample.

Despite the slow reaction kinetics, the impact of changes in the thermodynamic properties can be evaluated by analysis of the 300 °C desorption PCI plots given in Figure 8. Before measurements were undertaken, the CA/ $\text{MgH}_2$  sample was hydrogen cycled (desorbed for 18 h at 300 °C and then absorbed under 100 bar at 300 °C) to remove any traces of butane from the system that could lead to inflated pressure measurements. The bulk  $\text{MgH}_2$  sample was not hydrogen cycled and was held under a 50 bar of hydrogen pressure from room temperature to 300 °C to prevent decomposition in an attempt to maintain any microstructure before the PCI was collected.

The PCI analysis is made difficult due to particle size polydispersity in the CA/ $\text{MgH}_2$  sample. First, the bulk  $\text{MgH}_2$  sample behaves as expected with a flat equilibrium plateau at 1.70 bar. There is a slight equilibrium pressure reduction in the bulk PCI at low wt % (<1.0). This is an artifact that arises due to a decrease in desorption kinetics that occurs as the sample exhausts its hydrogen supply. For these data points, 3 h was insufficient to reach equilibrium (as indicated in the kinetic plots of each data point in the Supporting Information). The CA/ $\text{MgH}_2$  PCI exhibits a slightly sloped equilibrium plateau at marginally higher pressures ( $\leq 0.1$  bar) than the bulk. There is also a noticeable high-pressure slope at high wt % (A in Figure 8) that can result from nanoscale  $\text{MgH}_2$  particles with altered thermodynamics. It has been shown by the authors<sup>13</sup> that changes in  $\text{MgH}_2$  particle size lead to changes in thermodynamic properties ( $\Delta H$  and  $\Delta S$ ), causing higher-than-bulk equilibrium pressures. With a polydisperse sample, only a fraction of the  $\text{MgH}_2$  will exhibit particle sizes small enough to cause drastic thermodynamic changes. These thermodynamic changes can be detected by hydrogen equilibrium pressure changes in the system. When the system pressure is dropped during a desorption PCI measurement (A in Figure 8) to a pressure higher than the bulk equilibrium pressure (1.7 bar) but lower than the nano- $\text{MgH}_2$  equilibrium pressure, desorption will occur, but only from the small, thermodynamically altered  $\text{MgH}_2$  particles that have higher-than-bulk equilibrium pressures. Thus, the sloped region in the CA/ $\text{MgH}_2$  PCI can be attributed to extremely small  $\text{MgH}_2$  nanoparticles, likely the 2 nm  $\text{MgH}_2$  particles trapped in the 2 nm CA pores.

A temperature-programmed desorption (TPD) was undertaken on the hydrogen cycled CA/ $\text{MgH}_2$  sample as illustrated in Figure 9. The TPD profile displays a large  $\text{H}_2$  desorption peak centered about 340 °C, but there are also two minor desorption peaks at 150 and 250 °C. Hydrogen desorption at lower temperatures is an indication of either enhanced kinetics or enhanced thermodynamics. The nature of the low-temperature peaks cannot be discerned but their presence confirms that  $\text{MgH}_2$  particle size polydispersity is present within the sample. It is likely that the minor fraction of small  $\text{MgH}_2$  particles

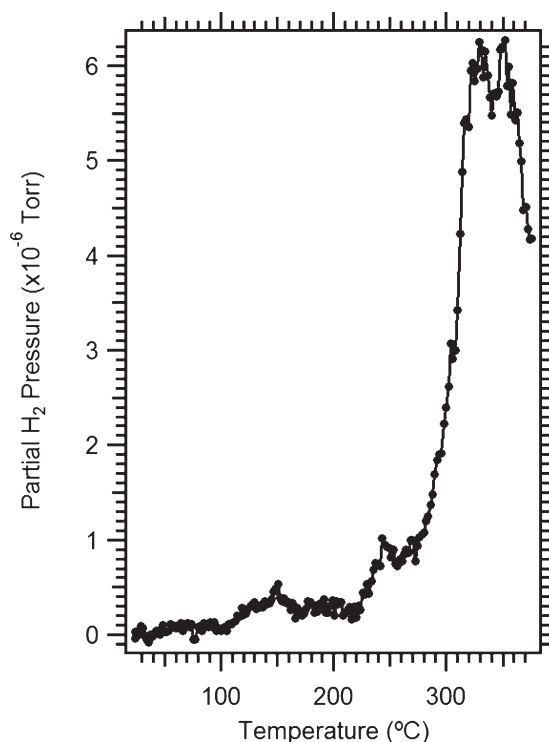


**Figure 9.** Temperature-programmed desorption (TPD) profile of hydrogen-cycled CA/ $\text{MgH}_2$  illustrating  $\text{H}_2$  desorption as temperature is ramped at 1 °C/min.

responsible for PCI deviations in Figure 8 also display hydrogen desorption at lower temperatures, shown by the minor  $\text{H}_2$  desorption peaks in Figure 9.

There is also a distinct difference between the PCI plot for CA/ $\text{MgH}_2$  and bulk  $\text{MgH}_2$  in the low wt % region of Figure 8 (region B) that is not an artifact of slow kinetics (as indicated by the kinetic curves for this sample in the Supporting Information). It is difficult to discern the physical cause of this PCI region where lowered equilibrium pressures are measured. However, both Wagemans et al.<sup>2</sup> and Cheung et al.<sup>3</sup> performed theoretical calculations on  $\text{MgH}_2$  nanoclusters. In addition to calculating the energy of Mg and  $\text{MgH}_2$  clusters, they also performed simulations on removing successive hydrogen molecules from the  $\text{MgH}_2$  nanoclusters. They found that, initially, these nanoclusters exhibited hydrogen desorption corresponding to a decrease in desorption enthalpy as compared to bulk  $\text{MgH}_2$  (i.e., an increased equilibrium pressure). With further hydrogen desorption, the remaining hydrogen within the nanocluster actually acts to stabilize the cluster and hinder further desorption. The result was that the last of the hydrogen molecules within the nanocluster actually had an increased enthalpy of desorption compared to bulk  $\text{MgH}_2$  (i.e., a decreased equilibrium pressure). Our experimental results seem to support these theoretical calculations by Wagemans et al.<sup>2</sup> and Cheung et al.<sup>3</sup>

In our system that comprises both nanosized and bulk like  $\text{MgH}_2$ , we would expect to initially see an increased equilibrium pressure (compared to bulk  $\text{MgH}_2$ ) at the beginning of desorption due to nanoparticles of  $\text{MgH}_2$ . Hydrogen will continue to desorb from these nanoparticles until the hydrogen-stabilized  $\text{MgH}_x$  clusters are more thermodynamically stable than bulk  $\text{MgH}_2$ . At this point, we would expect a flat plateau associated

with desorption from bulk  $\text{MgH}_2$  until it has exhausted its hydrogen. Finally, the remaining hydrogen associated with the hydrogen-stabilized nanoclusters will be desorbed, resulting in the knee associated with point B in Figure 8. We note here that a thorough treatment of the thermodynamics of the bulk  $\text{MgH}_2$  and  $\text{CA/MgH}_2$  requires PCI measurements performed at a number of temperatures. Thus far, the slow kinetics of the  $\text{CA/MgH}_2$  system have limited the PCI measurement to just one temperature.

## CONCLUSIONS

$\text{MgH}_2$  has been deposited within a carbon aerogel with a large quantity of 2 nm pores. There are 2 nm  $\text{MgH}_2$  particles present in the composite as shown by SAXS and TEM. However, a significant proportion of the  $\text{MgH}_2$  is greater than 10 nm in size (as shown by XRD), which is essentially bulk  $\text{MgH}_2$ . The polydispersity is apparent from the  $\text{CA/MgH}_2$  hydrogen pressure isotherm which displays features from both bulk and nano  $\text{MgH}_2$  systems.

The dibutylmagnesium deposition method must be improved in order to restrict  $\text{MgH}_2$  particles to the 2 nm pores within the carbon aerogel. The  $\text{MgH}_2$  particles must be relatively monodisperse for hydrogen sorption measurements to be able to easily detect and accurately measure thermodynamic changes with particle size. If a  $\text{CA/MgH}_2$  composite could be synthesized with 90–100% of the  $\text{MgH}_2$  trapped within the 2 nm CA pore network, then thermodynamic measurements could be reliably undertaken to accurately measure alterations to the enthalpy and entropy of  $\text{Mg-H}$  reactions with particle size. A monodisperse particle size may be obtained by suspending the  $\text{MgH}_2$  within a scaffold with a more uniform pore structure, such as mesoporous silica. However, unless major thermodynamic changes can be realized in the  $\text{Mg-H}$  system, it is not feasible for low-temperature operation. The  $\text{CA/MgH}_2$  system also suffers from poor kinetics, and with a large proportion of bulk  $\text{MgH}_2$  present in the material the particle size of  $\text{MgH}_2$  is unstable during heating. A more ideal  $\text{MgH}_2$  scaffold system may demonstrate better hydrogen sorption properties and the encapsulation of nanoparticles within scaffolds can be further applied to a range of different metal hydrides in order to study the thermodynamic properties of these materials as a function of particle size. The current research confirms that characterization of  $\text{CA/metal}$  hydride composites is possible and the techniques herein can be used to identify the presence of nanoscopic metal hydrides trapped within CA frameworks.

## ASSOCIATED CONTENT

**S Supporting Information.** Radial profiles and hydrogen desorption kinetic plots. This material is available free of charge via the Internet at <http://pubs.acs.org>.

## AUTHOR INFORMATION

### Corresponding Author

\*E-mail: [c.buckley@curtin.edu.au](mailto:c.buckley@curtin.edu.au).

## ACKNOWLEDGMENT

This research was undertaken on the SAXS/WAXS beamline at the Australian Synchrotron, Victoria, Australia. The authors acknowledge the facilities, scientific, and technical assistance of

the Australian Microscopy & Microanalysis Research Facility at the Centre for Microscopy, Characterization & Analysis, The University of Western Australia, a facility funded by The University, State and Commonwealth Governments. C.E.B. acknowledges the financial support of the Australian Research Council for ARC Discovery grant DP0877155, ARC REIF grant R00107962 2001, and ARC LIEF LE0989180 which enabled the laboratory-based SAXS and temperature-programmed desorption studies to be undertaken. Thanks to S. B. Wang for his assistance with the nitrogen adsorption measurements.

## REFERENCES

- (1) Kim, K. C.; Dai, B.; Johnson, J. K.; Sholl, D. S. *Nanotechnology* **2009**, *20*, 204001.
- (2) Wagemans, R. W. P.; van Lenthe, J. H.; de Jongh, P. E.; van Dillen, A. J.; de Jong, K. P. *J. Am. Chem. Soc.* **2005**, *127*, 16675.
- (3) Cheung, S.; Deng, W. Q.; vanDuin, A. C. T.; Goddard, W. A. *J. Phys. Chem. A* **2005**, *109*, 851.
- (4) Aguey-Zinsou, K.-F.; Ares-Fernández, J.-R. *Chem. Mater.* **2008**, *20*, 376.
- (5) Kalidindi, S. B.; Jagirdar, B. R. *Inorg. Chem.* **2009**, *48*, 4524.
- (6) Pundt, A. *Adv. Eng. Mater.* **2004**, *6*, 11.
- (7) de Jongh, P. E.; Wagemans, R. W. P.; Eggenhuisen, T. M.; Dauvillier, B. S.; Radstake, P. B.; Meeldijk, J. D.; Geus, J. W.; de Jong, K. P. *Chem. Mater.* **2007**, *19*, 6052.
- (8) Gross, A. F.; Ahn, C. C.; Van Atta, S. L.; Liu, P.; Vajo, J. J. *Nanotechnology* **2009**, *20*, 204005.
- (9) Bogerd, R.; Adelhelm, P.; Meeldijk, J. H.; de Jong, K. P.; de Jongh, P. E. *Nanotechnology* **2009**, *20*, 204019.
- (10) Nielsen, T. K.; Manickam, K.; Hirscher, M.; Besenbacher, F.; Jensen, T. R. *ACS Nano* **2009**, *3*, 3521.
- (11) Zhang, S.; Gross, A. F.; Van Atta, S. L. L.; Maribel; Liu, P.; Ahn, C. C.; Vajo, J. J.; Jensen, C. M. *Nanotechnology* **2009**, *20*, 204027.
- (12) Barkhordarian, G.; Klassen, T.; Bormann, R. *Scr. Mater.* **2003**, *49*, 213.
- (13) Paskevicius, M.; Sheppard, D. A.; Buckley, C. E. *J. Am. Chem. Soc.* **2010**, *132*, 5077.
- (14) Sheppard, D. A.; Paskevicius, M.; Buckley, C. E. *J. Alloys Compd.* **2010**, *492*, L72.
- (15) Tian, H. Y.; Buckley, C. E.; Mulé, S.; Paskevicius, M.; Dhal, B. B. *Nanotechnology* **2008**, *19*, 475605.
- (16) Cookson, D. J. SAXS15ID-A, software package for SAXS/WAXS data processing and analysis, 2006.
- (17) Zhang, F.; Ilavsky, J.; Long, G.; Quintana, J.; Allen, A.; Jemian, P. *Metall. Mater. Trans. A* **2010**, *41*, 1151.
- (18) Gray, E. M.; Cookson, D. J.; Blach, T. P. *J. Appl. Crystallogr.* **2006**, *39*, 850.
- (19) Coelho, A. A. *Topas User Manual*, 3.0th ed.; Bruker AXS GmbH: Karlsruhe, Germany, 2003; Version 3.0.
- (20) Dobrovolsky, V. D.; Ershova, O. G.; Solonin, Y. M.; Khyzhun, O. Y.; Paul-Boncour, V. *J. Alloys Compd.* **2008**, *465*, 177.
- (21) Ershova, O. G.; Dobrovolsky, V. D.; Solonin, Y. M.; Khyzhun, O. Y.; Koval, A. Y. *J. Alloys Compd.* **2008**, *464*, 212.
- (22) Yu, X. B.; Guo, Y. H.; Yang, Z. X.; Guo, Z. P.; Liu, H. K.; Dou, S. X. *Scr. Mater.* **2009**, *61*, 469.
- (23) Rongeat, C.; Llamas-Jansa, I.; Doppiu, S.; Deledda, S.; Borgschulte, A.; Schultz, L.; Gutfleisch, O. *J. Phys. Chem. B* **2007**, *111*, 13301.
- (24) Gutfleisch, O.; Schlorke-de Boer, N.; Ismail, N.; Herrich, M.; Walton, A.; Speight, J.; Harris, I. R.; Pratt, A. S.; Züttel, A. *J. Alloys Compd.* **2003**, *356–357*, 598.
- (25) Yu, X. B.; Guo, Y. H.; Yang, H.; Wu, Z.; Grant, D. M.; Walker, G. S. *J. Phys. Chem. C* **2009**, *113*, 5324.
- (26) Shao, H.; Wang, Y.; Xu, H.; Li, X. *Mater. Sci. Eng. B* **2004**, *110*, 221.

- (27) Lastoskie, C.; Gubbins, K. E.; Quirk, N. *J. Phys. Chem.* **1993**, 97, 4786.
- (28) Hilding, J.; Grulke, E. A.; Sinnott, S. B.; Qian, D.; Andrews, R.; Jagtoyen, M. *Langmuir* **2001**, 17, 7540.
- (29) Beaucage, G. *J. Appl. Crystallogr.* **1995**, 28, 717.
- (30) Griffith, W. L.; Triolo, R.; Compere, A. L. *Phys. Rev. A: Gen. Phys.* **1987**, 35, 2200.
- (31) Kline, S. R. *J. Appl. Crystallogr.* **2006**, 39, 895.
- (32) Lillo-Ródenas, M. A.; Guo, Z. X.; Aguey-Zinsou, K. F.; Cazorla-Amorós, D.; Linares-Solano, A. *Carbon* **2008**, 46, 126.